# Plane Wave Elastography: A Frequency-Domain Ultrasound Shear Wave Elastography Approach

Reza Khodayi-mehr<sup>1</sup>, Matthew W. Urban<sup>2</sup>, Michael M. Zavlanos<sup>1</sup>, and Wilkins Aguino<sup>1</sup>

<sup>1</sup> Department of Mechanical Engineering and Materials Science, Duke University, Durham, NC 27708, USA.

E-mail: {reza.khodayi.mehr, michael.zavlanos, wilkins.aquino}@duke.edu

<sup>2</sup> Department of Radiology, Mayo Clinic, Rochester, MN 55905, USA.

E-mail: urban.matthew@mayo.edu

March 2021, Patent Pending.

Abstract. In this paper, we propose Plane Wave Elastography (PWE), a novel ultrasound shear wave elastography (SWE) approach. Currently, commercial methods for SWE rely on directional filtering based on the prior knowledge of the wave propagation direction, to remove complicated wave patterns formed due to reflection and refraction. The result is a set of decomposed directional waves that are separately analyzed to construct shear modulus fields that are then combined through compounding. Instead, PWE relies on a rigorous representation of the wave propagation using the frequency-domain scalar wave equation to automatically select appropriate propagation directions and simultaneously reconstruct shear modulus fields. Specifically, assuming a homogeneous, isotropic, incompressible, linear-elastic medium, we represent the solution of the wave equation using a linear combination of plane waves propagating in arbitrary directions. Given this closed-form solution, we formulate the SWE problem as a nonlinear least-squares optimization problem which can be solved very efficiently. Through numerous phantom studies, we show that PWE can handle complicated waveforms without prior filtering and is competitive with state-of-the-art that requires prior filtering based on the knowledge of propagation directions.

Keywords: Ultrasound shear wave elastography (SWE), frequency-domain, scalar wave equation, plane wave, soft tissue, cancer diagnosis, lesion, phantom.

#### 1. Introduction

Soft tissue pathology is known to be correlated with change in tissue stiffness (Shiina et al. 2015). For instance, an increase in cellular density caused by malignant tumors, leads to an increased tissue stiffness (Mehrmohammadi et al. 2014, Barr & Zhang 2015, Gerber et al. 2017). Ultrasound elastography methods utilize this correlation by mechanically exciting the tissue and analyzing the subsequent motion to quantify its stiffness over a region of interest (ROI). Various clinical studies of such methods indicate their relevance for non-invasive monitoring and diagnosis of breast

and liver diseases among others (Athanasiou et al. 2010, Sigrist et al. 2017). In the case of breast cancer for instance, Itoh et al. (2006) used the quantitative ratio of lesion to background stiffness to determine the probability of malignancy, with higher contrasts indicating higher probability of the lesion being malignant.

Different ultrasound elastography techniques exist in the literature that can broadly be categorized into strain imaging and shear wave elastography (SWE) methods (Sigrist et al. 2017). Particularly, SWE methods generate and track shear waves that travel in the tissue with wave-speeds considerably smaller than their compressional counterparts (typically below  $10\,\mathrm{m/s}$ ) and have a low frequency content (below  $1500\,\mathrm{Hz}$ ). In these methods, the tissue excitation is achieved by a vertical displacement ( $1-20\,\mu\mathrm{m}$ ) using an acoustic radiation force (ARF) impulse from an ultrasound push beam, while high frame-rate ultrasound imaging techniques are used to track the induced shear wave (Deng et al. 2016). The supersonic shear imaging (SSI) method proposed by Bercoff et al. (2004), is one of the early works to outline the SWE approach and demonstrate its performance. On the other hand, the combpush ultrasound shear elastography (CUSE) of Song et al. (2012), is a more recent work that relies on simultaneous, parallel ARF beams and compounding to improve the quality of shear modulus estimations.

A number of different SWE algorithms have been proposed to estimate the shear modulus field from wave data. For instance, Bercoff et al. (2004) utilized the scalar wave equation along with the Fourier-transformed second-order derivatives of the scalar displacement field, while McLaughlin & Renzi (2006) proposed the use of a level-set function of wave-front arrival time. However, most currently used SWE methods, including the commercialized versions of SSI (Athanasiou et al. 2010) and CUSE (Denis et al. 2015) systems, utilize the time-of-flight (ToF) technique to estimate the wave-speed and corresponding shear modulus field (Tanter et al. 2008, Palmeri et al. 2008, Rouze et al. 2012, Song et al. 2012, Song et al. 2014, Carrascal et al. 2017). For instance, (Tanter et al. 2008, Song et al. 2014) utilize cross-correlation of the signal at nearby locations along the propagation direction (typically the lateral axis) to estimate the ToF, i.e., the time that it takes the wave-front to reach the second point from the first point. Alternatively, the time-to-peak of shear waveform can also be used to estimate the time-of-flight (Palmeri et al. 2008, Rouze et al. 2012, Carrascal et al. 2017). These methods assume that the medium is locally homogeneous, isotropic, incompressible, and linear-elastic (Palmeri et al. 2016) and rely on the prior knowledge of the propagation direction which is assumed to be perpendicular to the ARF push axis (Deng et al. 2016). This assumption is reasonable for 'directional' shear waves with flat wave-fronts; see (Sigrist et al. 2017) for details. We define a directional shear wave as a wave that has a clear dominant propagation direction.

In the presence of inhomogeneities like tumors, shear waves scatter due to reflection and refraction, violating the directionality assumption of ToF methods, which can lead to artifacts in the estimated shear modulus field (Deffieux et al. 2011, Parker et al. 2017). Directional filters are then necessary to remove the reflections and obtain directional waves (Manduca et al. 2003, Deffieux et al. 2011, Lipman et al. 2016). In their simplest form, directional filters are frequency-domain projections that only retain the wave components aligned with the given propagation direction; see (Deffieux et al. 2011) for details. They decompose the shear wave into a set of directional waves that can be separately analyzed via the ToF method. In addition to

<sup>1</sup> Shear modulus is one of the several quantities used to measure the stiffness of materials.

reflection and refraction, noise in the wave data can create artifacts in the estimated fields and a second radial filter is often necessary to improve the signal-to-noise ratio; see Appendix A for details. Ultimately, the shear modulus fields corresponding to different directions are combined through compounding (averaging) to obtain a final shear modulus field. When the direction of propagation is not aligned with the lateral axis, one dimensional (1D) analysis can overestimate the wave-speed. The fast shear compounding (FSC) method proposed by Song et al. (2014) utilizes a 2D analysis of wave-speed along with prior filtering for robust shear modulus estimation in inhomogeneous mediums. It extends the CUSE method (Song et al. 2012) to include multiple simultaneous ARF beams with arbitrary known directions. In Section 4, we compare our proposed approach to this method.

Another set of SWE methods exist that rely on similar assumptions but perform the wave-speed (phase velocity) analysis in the frequency domain (Chen et al. 2004, Chen et al. 2009, Budelli et al. 2016, van Sloun et al. 2017, Kijanka & Urban 2018). For instance, the local phase velocity imaging method proposed by Kijanka & Urban (2018), relies on short space 2D Fourier transform analysis of the wave data to extract the most dominant wavenumber within a homogeneous window. Assuming a directional propagation within the window, the phase velocity is estimated as the ratio of angular frequency to wavenumber. As discussed earlier, the assumption of directional propagation breaks down in the presence of inhomogeneities. Another family of frequency-domain methods utilize the elastodynamic partial differential equation (PDE) to rigorously model the shear wave propagation in this general form, automatically accounting for reflection and refraction. These methods can be classified into direct (Park & Maniatty 2006) and iterative (Eskandari et al. 2008, Ghosh et al. 2017, Aquino & Bonnet 2019) approaches. Direct methods, although more efficient, are sensitive to noise. The iterative methods on the other hand, despite versatility, are computationally demanding which has limited their practical utility.

It is known that for shear waves induced by ARF beams, the displacement component parallel to the push axis is dominant (Palmeri et al. 2016). Thus, we can use a scalar wave equation, instead of the elastodynamic PDE, to capture only the dominant shear wave component. Relying on this observation, we develop a novel frequency-domain SWE approach, called Plane Wave Elastography (PWE), that does not require the prior knowledge of propagation direction and is considerably more computationally efficient than the PDE-constrained approaches. More specifically, given a homogeneous subdomain within the ROI, we represent the solution of the scalar wave equation as a linear combination of plane waves with arbitrary propagation directions. Using this representation, we formulate the SWE problem as a nonlinear least-squares problem that can be efficiently solved for the constant wave-speed within the subdomain. The PWE method relaxes the need for prior denoising by relying on a regularized least-squares formulation and directional filtering through automatic selection of dominant plane waves and does not require the post-processing step of compounding. Moreover, the optimal mean squared error (MSE) is an indicator of how closely the data conforms to the scalar wave equation. This can be used to provide feedback on the quality of reconstruction since higher levels of MSE indicate deviation from the wave model due possibly to noise. Finally, when the geometry of inclusions is known, e.g., from B-mode images, the PWE method can reconstruct the shear modulus field by a single solve for each homogeneous subdomain.

In summary, compared to the common SWE methods, our approach (i) has competitive reconstruction performance without relying on prior denoising, directional filtering and the prior knowledge of the propagation direction, or the need for compounding, (ii) provides feedback on quality of reconstructions using the MSE, and (iii) can take advantage of the prior knowledge of the inclusion geometry, if available, to speed up computations and improve the estimation contrast.

A closely related approach to PWE was proposed by Baghani et al. (2011) for magnetic resonance elastography (MRE). In their approach, the solution of an elastodynamics PDE was approximated using a set of plane wave expansions in a similar vein as in our PWE approach. However, their work considers a vector-valued problem in which all components of displacements are required. This is not directly applicable to an ultrasound modality where only one component of displacement is usually available. Our approach improves upon this previously proposed method in several key aspects by: i) adapting the plane-wave expansion to the scalar wave equation, thus enabling the use of ultrasound tracking, ii) decreasing the ensuing computational cost, iii) adding a multi-frequency treatment and, iv) incorporating the systematic and consistent treatment of noise through regularization which enables more accurate reconstructions without prior filtering. A comparison of the approach proposed by Baghani et al. (2011) to other popular MRE techniques is given by Honarvar et al. (2017). Finally, Parker et al. (2017) also utilized a plane-wave expansion, but to model narrow-band reverberant wave fields in which, no propagation direction is dominant. This does not apply to the ARF-based SWE problem considered here which often has a few dominant directions.

The remainder of this paper is organized as follows. In Section 2, we formulate the SWE problem and in Section 3, we present the PWE approach to solve it. In Section 4, we present various phantom studies demonstrating the performance of the PWE method. Section 5 is dedicated to discussing various aspects of our method highlighting its strengths and weaknesses, and Section 6 concludes the paper.

## 2. Problem Formulation

#### 2.1. Scalar Wave Equation

Let  $\Omega_{\text{ROI}} \subset \mathbb{R}^2$  denote the region of interest (ROI) and consider a shear wave propagating in  $\Omega_{\text{ROI}}$  in response to one or a set of acoustic radiation force (ARF) push beams applied outside  $\Omega_{\text{ROI}}$ ; let  $\hat{\mathbf{u}}(t,\mathbf{x}):[0,T]\times\Omega_{\text{ROI}}\to\mathbb{R}^2$  denote the in-plane displacement at time t and point  $\mathbf{x}$  due to this shear wave. Ultrasound transducers often only measure the dominant component of the displacement parallel to the push directions; let  $\hat{u}(t,\mathbf{x})=\hat{\mathbf{u}}_d(t,\mathbf{x})$  denote this dominant component.

Assuming that the medium is isotropic, incompressible, and linear-elastic (Palmeri et al. 2016), and assuming that the ARF push beams are applied outside the ROI, we can represent the propagation of the shear wave in  $\Omega_{\rm ROI}$  using the scalar wave equation

$$\rho \, \ddot{\hat{u}} = \nabla \cdot (\mu_f \nabla \hat{u}),$$

where  $\rho = 1000 \,\mathrm{kg/m^3}$  is the mass density of the soft tissue and  $\mu_f : \Omega_{\mathrm{ROI}} \to \mathbb{R}_{++}$  is the shear modulus field;  $\mathbb{R}_{++}$  denotes the positive real numbers. Note that the shear modulus is related to the shear wave-speed  $c_f : \Omega_{\mathrm{ROI}} \to \mathbb{R}_{++}$  as

$$\mu_f(\mathbf{x}) = \rho \, c_f^2(\mathbf{x}). \tag{1}$$

Let  $u: \Omega_{ROI} \to \mathbb{C}$  denote the Fourier transformed signal with respect to the temporal coordinate at a frequency  $\omega$ , i.e.,  $u(\mathbf{x}; \omega) = \mathcal{F}\{\hat{u}(t, \mathbf{x})\}$ . Then, given frequency  $\omega$ , the

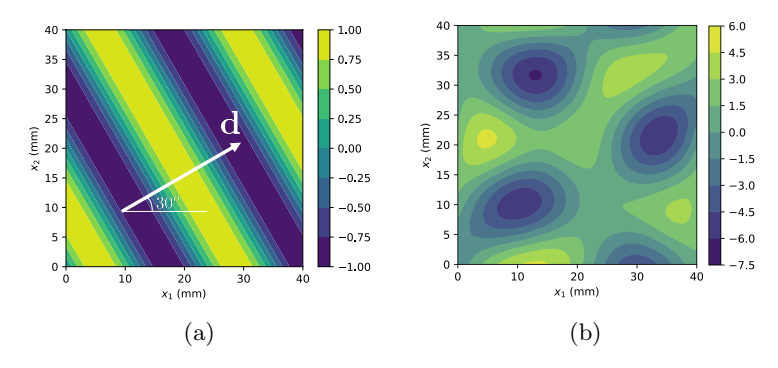


Figure 1: A plane wave and a shear wave field obtained by superposing plane waves within a homogeneous subdomain  $\Omega = [0,40] \times [0,40] \, \text{mm}^2$  with wave-speed  $c=5 \, \text{m/s}$  at frequency  $\omega = 500\pi \, \text{rad/s}$ . (a) Fig. 1a shows the imaginary component of the plane wave (4) with  $\mathbf{d} = [\cos(30^o), \sin(30^o)]$ . (b) Fig. 1b depicts the imaginary component of the shear wave obtained from (3) by superposing  $n_b = 12$  plane waves with  $30^o$  angular spacing and random coefficients with arbitrary units.

scalar wave equation can be written in the frequency-domain as

$$\rho \,\omega^2 u + \nabla \cdot (\mu_f \nabla u) = 0. \tag{2}$$

Consider a homogeneous subdomain  $\Omega \subset \Omega_{ROI}$  with constant shear modulus  $\mu = \mu_f(\mathbf{x} \in \Omega)$ . Then, we can write solutions to the scalar wave equation (2) in  $\Omega$  as a linear combination of basis functions  $\phi_j(\mathbf{x}) : \Omega \to \mathbb{C}$ , i.e.,

$$u(\mathbf{x}) = \sum_{j=1}^{n_b} a_j \,\phi_j(\mathbf{x}),\tag{3}$$

where  $n_b$  is the number of basis functions,  $a_j \in \mathbb{C}$ , and the basis functions  $\phi_j(\mathbf{x})$  are plane waves explicitly given by

$$\phi_j(\mathbf{x}) = \exp\left(\mathbf{i} \frac{\omega}{c} \, \mathbf{d}_j \cdot \mathbf{x}\right). \tag{4}$$

In this expression, **i** denotes the unit imaginary number,  $c = c_f(\mathbf{x} \in \Omega)$  is the constant wave-speed within the homogeneous subdomain  $\Omega$ , and  $\mathbf{d}_j \in \mathbb{R}^2$  are unit direction vectors of propagation, i.e.,  $\|\mathbf{d}_j\| = 1$ , where  $\|\cdot\|$  denotes the Euclidean  $\ell_2$ -norm. Fig. 1 depicts a plane wave of form (4) and a shear wave obtained by superposing  $n_b = 12$  plane wave bases according to (3). By increasing  $n_b$  and appropriate selection of coefficients  $a_j$  in (3), we can approximate any solution to the scalar wave equation (2) arbitrarily close in a normed sense (Colton & Kress 2001).

## 2.2. Shear Wave Elastography Problem

Let  $\hat{\mathbf{y}}(t) \in \mathbb{R}^m$  denote the temporal signal measured at m points  $\mathbf{x}_i \in \Omega$  for  $i \in \{1, ..., m\}$  and  $\mathbf{y} \in \mathbb{C}^m$  denote the corresponding (discrete) Fourier transformed signal at a frequency  $\omega$ . The objective of the elastography problem then is to find the constant shear modulus  $\mu$  or equivalently the wave-speed c within the homogeneous subdomain  $\Omega$ . Given the basis expansion (3), we can formulate this problem as a nonlinear least-squares optimization problem as follows:

$$\min_{c, \mathbf{a}} \frac{1}{m} \| \mathbf{\Phi}(c) \mathbf{a} - \mathbf{y} \|^2, \tag{5}$$

where  $\mathbf{a} = [a_1, \dots, a_{n_b}]$  is the vector of coefficients and  $\mathbf{\Phi} \in \mathbb{C}^{m \times n_b}$  is the design matrix with

$$\mathbf{\Phi}_{ij} = \phi_j(\mathbf{x}_i) \tag{6}$$

for  $i \in \{1, ..., m\}$  and  $j \in \{1, ..., n_b\}$ .

Whenever the number of measurements m is less than the number of bases  $n_b$ , the optimization problem (5) is ill-posed. Furthermore, often the measured signal is contaminated with noise and we do not want the solution (3) of the wave equation (2) to perfectly match the measurements  $\mathbf{y}$ . To address these challenges, we add a regularization term to (5) that improves stability and allows us to control how closely we fit the data:

$$\min_{c, \mathbf{a}} \frac{1}{m} \left\| \mathbf{\Phi}(c) \mathbf{a} - \mathbf{y} \right\|^2 + \tau \left\| \mathbf{a} \right\|^2,$$

where  $\tau \in \mathbb{R}_{++}$  is the regularization parameter. Note that the use of regularization encourages selection of a subset of plane waves and helps distinguish dominant propagation directions by penalizing nonzero coefficients  $a_i$ .

So far we have utilized the data at a single frequency  $\omega$ . It is often necessary to consider a set of dominant frequencies  $\{\omega_1,\ldots,\omega_{n_\omega}\}$ , where  $n_\omega$  denotes the number of frequencies. Given measurements  $\mathbf{y}_k \in \mathbb{C}^m$  for  $k \in \{1,\ldots,n_\omega\}$ , we use the linear expansion (3) with coefficients  $\mathbf{a}_k$  to represent the solution of the scalar wave equation (2) at frequency  $\omega_k$ . Then, the corresponding elastography problem is given by

$$\min_{c} \sum_{k=1}^{n_{\omega}} \min_{\mathbf{a}_{k}} \frac{1}{m} \left\| \mathbf{\Phi}_{k}(c) \mathbf{a}_{k} - \mathbf{y}_{k} \right\|^{2} + \tau \left\| \mathbf{a}_{k} \right\|^{2}. \tag{7}$$

Shear wave data are often calculated from the in-phase-quadrature data using an autocorrelation algorithm (Kasai et al. 1985) and are given as particle *velocity* and not displacement. Noting that  $\mathcal{F}\left\{\dot{\hat{u}}\right\} = \mathbf{i}\,\omega\mathcal{F}\left\{\hat{u}\right\} = \mathbf{i}\,\omega\,u$ , we can represent the (discrete) Fourier transformed velocity data with an expansion similar to (3) and scaled coefficients. Therefore, regardless of whether displacement or velocity data are used, the elastography problem is formulated as (7). In the next section, we discuss an efficient approach to solve this optimization problem.

# 3. Plane Wave Elastography

# 3.1. Solution to the Elastography Problem in a Homogeneous Subdomain

Solving the optimization problem (7) can be challenging due to nonlinearity; see Appendix B. However, for a fixed wave-speed c, (7) is a standard  $\ell_2$ -regularized least-squares problem whose solution for each frequency, is given in closed-form by

$$\mathbf{a}_k^*(c) = \left(\frac{1}{m}\mathbf{\Phi}_k(c)^H\mathbf{\Phi}_k(c) + \tau \mathbf{I}\right)^{-1}\mathbf{\Phi}_k(c)^H\mathbf{y}_k,\tag{8}$$

where  $\mathbf{I} \in \mathbb{R}^{n_b \times n_b}$  is the identity matrix and the superscript H denotes the conjugate transpose operator. Given this closed-form expression and since within the homogeneous subdomain  $\Omega$ , the wave-speed c is a constant scalar, we can utilize a global search algorithm or a simple discretization method to find the optimal wave-speed as

$$c^* = \underset{c \in [c_{\min}, c_{\max}]}{\operatorname{argmin}} \sum_{k=1}^{n_{\omega}} \frac{1}{m} \| \mathbf{\Phi}_k(c) \, \mathbf{a}_k^*(c) - \mathbf{y}_k \|^2 + \tau \| \mathbf{a}_k^*(c) \|^2,$$
 (9)

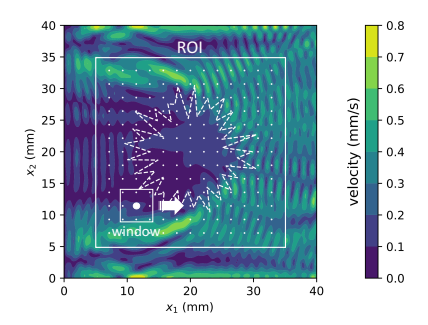


Figure 2: Schematic of the PWE algorithm to estimate the shear modulus field in an inhomogeneous ROI. The white dots depict  $n_s$  discretization points within the ROI. The main idea is to estimate the field at each discretization point by a window  $\Omega_l$  of size  $w \times w$  centered at that point. The contour plot shows the magnitude of Fourier transformed data at 800 Hz for the digital phantom of Section 4.1 as an example, where the white dashed lines delineate the boundary of the inclusion. In practice, the PWE Algorithm 1 utilizes  $n_\omega$  dominant frequencies within each window.

where  $c_{\min}, c_{\max} \in \mathbb{R}_{++}$  are the lower-bound and upper-bound on the wave-speed and  $\mathbf{a}_{k}^{*}(c)$  is the optimal regularized least-squares solution (8) for a given wave-speed c.

Assume that we use a limited number of basis functions  $n_b$  and frequencies  $n_\omega$  along with appropriate regularization to prevent overfitting the noise. Then, the value of the least-squares term corresponding to the optimal wave-speed  $c^*$  can be used as a measure of conformity of the data to the scalar wave equation (2); the smaller the least-squares error, the closer the data is to the underlying physics. Thus, we can use this feedback to evaluate the quality of reconstruction. Particularly, we use the mean squared error (MSE), given by

$$MSE = \frac{1}{m n_{\omega}} \sum_{k=1}^{n_{\omega}} \| \mathbf{\Phi}_k(c^*) \mathbf{a}_k^*(c^*) - \mathbf{y}_k \|^2,$$
 (10)

as a measure of the quality of reconstruction in  $\Omega$ .

# 3.2. Plane Wave Elastography Algorithm

Our solution in Section 3.1 was for a homogeneous subdomain  $\Omega$  with constant shear modulus. To estimate the shear modulus field  $\mu_f(\mathbf{x})$  over an inhomogeneous ROI, we discretize the ROI into  $n_s$  grid points and use windows of size  $w \in \mathbb{R}_{++}$  with constant shear moduli. Particularly, for a point  $\mathbf{x}_l \in \Omega_{\text{ROI}}$  we define a window (subdomain)  $\Omega_l$  as

$$\Omega_l = \mathbf{x}_l + \left[ -\frac{w}{2}, \frac{w}{2} \right] \times \left[ -\frac{w}{2}, \frac{w}{2} \right]. \tag{11}$$

We solve (9) to estimate the wave-speed  $c_l$  and the corresponding shear modulus  $\mu_l$  within  $\Omega_l$  and assign the value to point  $\mathbf{x}_l$ , constructing in this way, a discretized vector of estimations  $\boldsymbol{\mu} \in \mathbb{R}^{n_s}_{++}$  for the shear modulus field  $\mu_f(\mathbf{x})$ ; see Fig. 2.

The Plane Wave Elastography (PWE) approach is summarized in Algorithm 1. The algorithm starts by requiring the  $n_s$  discretization points and window size w, as well as the number of plane wave basis functions  $n_b$  and dominant frequencies  $n_\omega$ . In line 2, given the (discrete) Fourier transformed displacement signal  $\mathbf{y}_{\text{ROI}}$ , it selects the regularization parameter  $\tau$ ; see Section 3.3 for details. Then, the algorithm loops over the  $n_s$  discrete points within the ROI. In line 4, given the measurements within window

#### Algorithm 1 Plane Wave Elastography Algorithm

```
Require: Discretization of the ROI and window size w;
```

**Require:** Number of basis functions  $n_b$  and dominant frequencies  $n_{\omega}$ ;

**Require:** Shear wave measurement signal  $\hat{\mathbf{y}}_{ROI}(t)$ ;

- 1: Compute the Fourier transformed data  $\mathbf{y}_{ROI}$ ;
- 2: Select the regularization parameter  $\tau$ ;
- 3: **for**  $l \in \{1, ..., n_s\}$  **do**
- 4: Get measurements  $\mathbf{y}_k \in \mathbb{C}^m$  within window  $\Omega_l$  for dominant frequencies  $k \in \{1, \ldots, n_{\omega}\}$ ;
- 5: Compute the wave-speed  $c_l$  from (9) and the corresponding MSE value from (10);
- 6: end for
- 7: Compute the shear modulus vector  $\mu \in \mathbb{R}^{n_s}_{++}$  from (1);
- 8: Return  $\mu$  and the corresponding MSE vector (10);

 $\Omega_l$  for  $l \in \{1, \ldots, n_s\}$ , it extracts the  $n_\omega$  dominant frequencies contributing the highest amount of energy to the Fourier spectrum, and the corresponding measurements  $\mathbf{y}_k \in \mathbb{C}^m$  for  $k \in \{1, \ldots, n_\omega\}$ . Then, in line 5, it computes the constant wave-speed  $c_l$  for window  $\Omega_l$  from (9) and the corresponding MSE from (10). In line 7,  $\boldsymbol{\mu}$  collects the estimated shear moduli corresponding to all discretization points  $\mathbf{x}_l$  within the ROI. Given  $\boldsymbol{\mu}$ , we can approximate the shear modulus field  $\mu_f(\mathbf{x})$  at any point  $\mathbf{x}$  via interpolation.

#### 3.3. Parameter Selection

Next, we discuss the important parameters that affect the performance of the PWE Algorithm 1. As discussed in Section 1, an important advantage of the PWE approach is that it does not rely on the directionality of the propagation, due to the plane wave representation in (3). In the absence of any prior knowledge on the directionality of the propagation, we choose the directions  $\mathbf{d}_{j}$  to uniformly sample  $[0, 2\pi]$ , i.e.,

$$\mathbf{d}_{j} = \left[\cos\left(2\pi \frac{j}{n_{b}}\right), \sin\left(2\pi \frac{j}{n_{b}}\right)\right]. \tag{12}$$

As we demonstrate in Section 4, in practice often  $n_b \leq 12$  directions are sufficient to resolve the propagating waves.

An important parameter for the PWE method is the number of dominant frequencies  $n_{\omega}$ . In principle, increasing  $n_{\omega}$  adds more information and leads to more accurate reconstructions. However, one should take caution not to include very high frequencies with unfavorable signal to noise ratios, i.e.,  $\omega_{\max} = 2\pi f_{\max}$  must be upper-bounded, where  $f_{\max}$  is the corresponding frequency in Hertz. Another important parameter is the lower-bound  $\omega_{\min} = 2\pi f_{\min}$  on dominant frequencies, which determines the longest wavelength  $\lambda_{\max}$  in the data. More specifically,  $\lambda_{\max} = \hat{c}_{\max}/f_{\min}$  where  $\hat{c}_{\max}$  is the unknown maximum wave-speed in the ROI. As a general rule of thumb, for data with a high signal-to-noise ratio (SNR), the window size must be larger than  $\lambda_{\max}/5$  to ensure that waves can be resolved with a window of size w. Note that w also determines the number of measurements m used to estimate the wave-speed in each subdomain  $\Omega_l$ . Using at least  $m > n_b$  measurements is required to ensure that the design matrix (6) is well-conditioned. When the SNR is low, larger values of w should be used to ensure that the measurements contain adequate information about

the unknown wave speed. In practice, the range of dominant frequencies  $[f_{\min}, f_{\max}]$  and the spatial resolution of measurements are fixed for a given shear wave data but both  $\hat{c}_{\max}$  and SNR are unknown. As a result, for best reconstructions we might need to adjust w. The quality of reconstructions by the PWE Algorithm 1 are often better for data with higher SNR and  $f_{\min}$  for which smaller values of w can be used.

When data is noisy, a major parameter that affects the reconstruction is the regularization parameter  $\tau$ . As discussed in Section 2.2, proper selection of  $\tau$  allows us to simultaneously perform filtering and reconstruction. In this paper, we utilize the L-curve approach to select  $\tau$ . This involves plotting the regularization term  $\sum_{k=1}^{n_{\omega}} \|\mathbf{a}_{k}^{*}\|^{2}$  in (9) versus the sum-of-squares value (a constant multiple of MSE (10)) as a function of  $\tau$  and selecting the regularization parameter corresponding to the point of maximum curvature in the L-curve; see (Hansen 2010). In Section 4.4, we present parameter study results to further clarify the discussion of this section.

# 3.4. Prior Knowledge of ROI Geometry

In practice, the prior knowledge of the location and shape of inclusions (inhomogeneities) within the ROI might be available, e.g., from B-mode images. In that case, we can estimate the shear modulus field with a considerably fewer solves than what is needed in Algorithm 1, which requires one solution per discretization point. Particularly, consider a decomposition of the ROI into  $n_s$  non-overlapping subdomains such that  $\Omega_{\text{ROI}} = \bigcup_{l=1}^{n_s} \Omega_l$ , where within  $\Omega_l$  the shear modulus is constant and equal to  $\mu_l$ . Then, solving (9) with measurements belonging to  $\Omega_l$ , we obtain an estimate of the wave-speed  $c_l$  and the corresponding shear modulus  $\mu_l$  from (1) and we can estimate the shear modulus field as

$$\mu_f(\mathbf{x}) = \sum_{l=1}^{n_s} \mu_l \, \mathbf{1}_{\Omega_l}(\mathbf{x}),\tag{13}$$

where the indicator function  $\mathbf{1}_{\Omega_l}(\mathbf{x}) = 1$  if  $\mathbf{x} \in \Omega_l$  and is zero otherwise.

## 4. Experiments

In this section, we present phantom studies to demonstrate the performance of the PWE Algorithm 1. Particularly, we first study a digital phantom with a complex inclusion mimicking a malignant tumor to induce reflections and refractions, demonstrating the ability of PWE to resolve complicated wave patterns without prior filtering. Then, we consider two categories of phantom experiments. The first category involves four simultaneous ARF push beams applied using a curved-array ultrasound transducer at different angles and validates in practice, the ability of the PWE approach to resolve waves traveling at unknown arbitrary directions. We also consider the more common case of two parallel push beams generated by a linear transducer. For these phantom experiments, we calculate the shear wave data from the in-phase-quadrature data using an autocorrelation algorithm (Kasai et al. 1985). Finally, we study the effect of various parameters on the performance of PWE to further illustrate the discussion of Section 3.3.

In each case, in addition to nominal values, we report reconstructions by the fast shear compounding (FSC) method, proposed by Song et al. (2014), to validate the

<sup>2</sup> Due to the extra minimization with respect to wave-speed in (7), the curve generated in this way is not exactly the L-curve but as we show in Section 4, this version can still be used to select appropriate regularization parameters.

PWE reconstructions and demonstrate that PWE performs at least as well as the state-of-the-art<sup>3</sup>, even though it does not require prior filtering or post-processing. Note that the FSC method strongly relies on directional filtering to ensure the directionality of the waves and radial filtering in the spatial frequency domain, to enhance the SNR; see Appendix A for details. In the case of a multi-push excitation, the FSC method reconstructs shear modulus fields individually for each filtered direction and then uses compounding to combine the reconstructions. In the following, we fine-tune the parameters of this method for best possible reconstructions. We particularly report the window size defined similar to (11), and the patch size which is the distance between pairs of points used for cross-correlation to determine the time-of-flight; see (Song et al. 2014) for details.

To measure the reconstruction performance, we report the average shear moduli  $\mu_b = \operatorname{avg}(\mu_{\Omega_b})$  and  $\mu_i = \operatorname{avg}(\mu_{\Omega_i})$  over the background  $\Omega_b$  and inclusion  $\Omega_i$  along with the standard deviations  $\operatorname{std}(\mu_{\Omega_b})$  and  $\operatorname{std}(\mu_{\Omega_i})$ , where  $\mu_{\Omega_b}$  and  $\mu_{\Omega_i}$  denote the estimated shear modulus vector  $\mu$  confined to subdomains  $\Omega_b$  and  $\Omega_i$ , respectively. For phantom experiments, we obtain an approximation of the inclusion geometry from B-mode images. We also report the contrast-to-noise ratio (CNR), defined as

$$CNR = 20 \log_{10} \frac{\left| \operatorname{avg}(\boldsymbol{\mu}_{\Omega_b}) - \operatorname{avg}(\boldsymbol{\mu}_{\Omega_i}) \right|}{\sqrt{\operatorname{std}^2(\boldsymbol{\mu}_{\Omega_b}) + \operatorname{std}^2(\boldsymbol{\mu}_{\Omega_i})}}.$$
(14)

Throughout this section, for PWE reconstructions we use  $n_{\omega}=10$  dominant frequencies and  $n_b=12$  basis functions and set the maximum frequency to  $f_{\rm max}=1500\,{\rm Hz}$ ; see Section 4.4 for the reasoning behind this selection. We also set the wavespeed bounds in (9) to  $c_{\rm min}=1\,{\rm m/s}$  and  $c_{\rm max}=10\,{\rm m/s}$ , which is a reasonable range for soft tissue (Sarvazyan et al. 2013). Moreover, to conform to the ultrasound coordinate system convention, where the transducer is located on top, in the following plots we use axial or depth axis z and lateral axis x with the origin located on the top-left corner.

## 4.1. Single-push Digital Phantom

In this section, we study the performance of PWE for a  $40\,\mathrm{mm}\times40\,\mathrm{mm}$  digital phantom with an inclusion mimicking a malignant tumor, see e.g. (Liu et al. 2016, Fig. 1), with a background shear modulus of  $5\,\mathrm{kPa}$  and inclusion shear modulus of  $19\,\mathrm{kPa}$ ; see Fig. 3 for the shape of the inclusion. To simulate the shear wave propagation, we discretize the domain with a spatial interval of  $\Delta x = 250\,\mathrm{\mu m}$  and temporal stepsize of  $\Delta t = 100\,\mathrm{\mu s}$  and solve the 2D incompressible elastodynamic PDE (Aquino & Bonnet 2019) in FENICS (Alnaes et al. 2015) using a mixed finite element method, subject to an unfocused ARF impulse modeled by a sinusoidal traction with frequency of  $1000\,\mathrm{Hz}$  along the right side of the domain. The duration of the impulse was  $10\,\Delta t$  and the duration of the simulation was  $20\,\mathrm{ms}$ . In the following, we study the performance of PWE without and with noise over a  $30\,\mathrm{mm}\times30\,\mathrm{mm}$  ROI.

The plots in the first row of Fig. 3 show the reconstructions for noiseless data. For PWE results, we set the minimum frequency to  $f_{\rm min} = 500\,{\rm Hz}$  after inspecting the Fourier transfer spectrum, and the window size to  $w = 1.50\,{\rm mm}$ , accordingly. Because the data is noiseless, a wide range of values are appropriate for the regularization

3 FSC method is commercially used on General Electric LOGIQ E9 SWE system (Song et al. 2015).

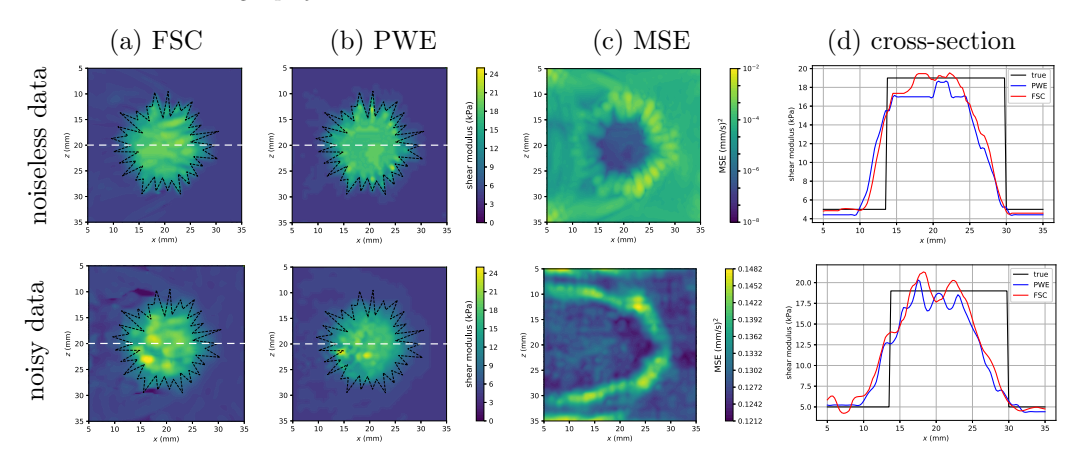


Figure 3: PWE and FSC reconstructions for the digital phantom. Inclusion boundaries are delineated by black dashed lines. The first row corresponds to noiseless data while the second row corresponds to data contaminated with additive Gaussian noise. Column (a) includes the reconstructions obtained using the FSC method whereas column (b) includes the PWE reconstructions. Column (c) depicts the MSE fields (10) for the PWE reconstructions. In column (d), we compare the ground-truth shear modulus with the estimated values along the horizontal line passing through the center of the ROI, depicted by the white dashed lines in the shear modulus contour plots.

parameter; we set  $\tau = 10^{-4}$  from the L-curve analysis. From the PWE reconstruction, the average background and inclusion shear moduli are  $\mu_b = 4.89 \pm 1.27 \,\mathrm{kPa}$  and  $\mu_i = 14.76 \pm 3.36 \,\mathrm{kPa}$ , respectively. The contrast-to-noise ratio is CNR = 8.78 dB. Referring to the MSE field in column (c) of Fig. 3, observe that the regions at the boundary of inclusion and background have the highest MSE values (10) since at those regions, the assumption of homogeneity breaks down (the windows cover parts of both the inclusion and background). Moreover, generally the MSE values are smaller inside the inclusion indicating better agreement with the wave equation (2). This could be due to the fact that the inclusion is farther away from the ARF push-beam location; because the ARF is not modeled in (2), regions close to it will have higher discrepancy with the model and thus, higher MSE values. For the FSC method (Song et al. 2014), we get  $\mu_b = 5.15 \pm 1.25 \,\mathrm{kPa}$  and  $\mu_i = 15.12 \pm 3.28 \,\mathrm{kPa}$  and CNR = 9.08 dB, where we use a window size of 1.00 mm and patch size of 0.75 mm. Referring to cross-section plots in column (d) of Fig. 3, observe that the inclusion edges are smoothed out due to windowing, resulting in slightly skewed estimations compared to the ground truth.

To investigate the effect of noise, we contaminated the simulated shear wave data with additive Gaussian noise decreasing the signal-to-noise ratio to SNR =  $-9.05\,\mathrm{dB}$ . The plots in the second row of Fig. 3 show the reconstructions for this case. In the presence of noise, larger window sizes are required for the same minimum frequency  $f_{\min} = 500\,\mathrm{Hz}$ , to ensure that more measurements with adequate information content are included for reasonable reconstructions. Using  $w = 5.50\,\mathrm{mm}$  and  $\tau = 10^{-2}$  from the L-curve analysis, we get  $\mu_b = 5.09 \pm 1.20\,\mathrm{kPa}$  and  $\mu_i = 13.35 \pm 3.71\,\mathrm{kPa}$ , and CNR =  $6.52\,\mathrm{dB}$  from the PWE method. Referring to the MSE feedback in column (c), we can see that the MSE values are orders of magnitude higher in this case indicating

<sup>4</sup> Although Gaussian noise is not an accurate model of the ultrasound noise, it has been used in the literature regardless; see e.g., (Kijanka et al. 2018). In the next sections, we study phantom experiments that inherently contain realistic ultrasound noise.

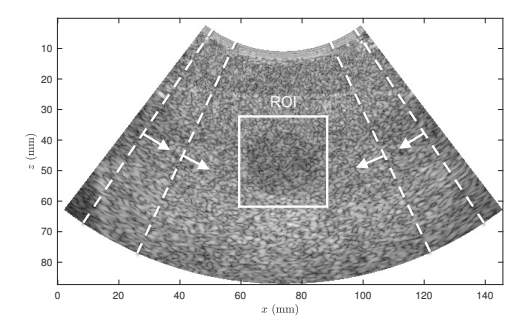


Figure 4: The geometry of the Type IV CIRS phantom and the location of the 20 mm spherical inclusion for multi-push data. The dashed lines delineate the approximate orientation of the four push beams while the arrows show the directions of propagation and the approximate focal depths (40 mm) along the push beam axes. Finally, the square box depicts the 30 mm×30 mm ROI.

considerable disagreement with the wave equation (2). Because the noise is uniformly added across all spatial locations, the MSE values are very close throughout the ROI. Finally using the FSC method, we get  $\mu_b = 5.42 \pm 1.52$  kPa and  $\mu_i = 14.87 \pm 3.97$  kPa and CNR = 6.94 dB, where we use a window size of 2.00 mm and patch size of 1.75 mm. Note that prior filtering to improve the SNR is essential to obtaining reasonable reconstructions using the FSC method in the presence of noise.

## 4.2. Multi-push CIRS Phantom

Next, we consider a phantom with nominal background shear modulus of 8.33 kPa and a single spherical inclusion with shear modulus of 26.66 kPa and diameter of 20 mm (Model 049, CIRS, Inc., Norfolk, VA), excited by four simultaneous ARF push beams transmitted by a C5-2 curved-array transducer (Verasonics, Inc., Kirkland, WA) and measured with a research scanner (V1, Verasonics, Inc., Kirkland, WA). Each push beam used 16 elements, and the beams were moved to the edge of the transducer such that two beams were formed on the extreme left and right sides of the array and 64 elements in the center were inactive. We study two ARF push configurations with push frequency of 4.09 MHz: (i) one push with duration of 400 µs; (ii) four repeated pushes of duration 200 µs separated by 800 µs of waiting, generating a repeated push of 1000 Hz. This repeated push is intended to excite a wider frequency range (Urban & Greenleaf 2008). A movie of the vertical shear wave velocity component generated under these two push configurations can be found in (Khodayi-mehr et al. 2020). Fig. 4 depicts the geometry of the phantom and the  $30 \,\mathrm{mm} \times 30 \,\mathrm{mm}$  ROI along with the approximate location of the inclusion and the focused push beams (focal depth is 40 mm). Note that the prior knowledge of the push beam angles and equivalently the propagation directions, is not required for PWE. The spatial spacing of the shear wave data was 240 µm while the temporal interval was 360 µs. The duration of the signal was  $20 \,\mathrm{ms}$ .

The plots in the first row of Fig. 5 depict the reconstructions for the push configuration (i). For the PWE results in column (b), we use  $f_{\min} = 300 \,\text{Hz}$  and  $w = 7.67 \,\text{mm} \approx 32 \times 240 \,\mu\text{m}$  and set  $n_b = 12$  as before. Note that  $n_b = 12$  basis functions are sufficient to reconstruct the field even though the PWE Algorithm 1 is unaware of the propagation directions. We use a regularization parameter of  $\tau = 10^{-2}$ ,

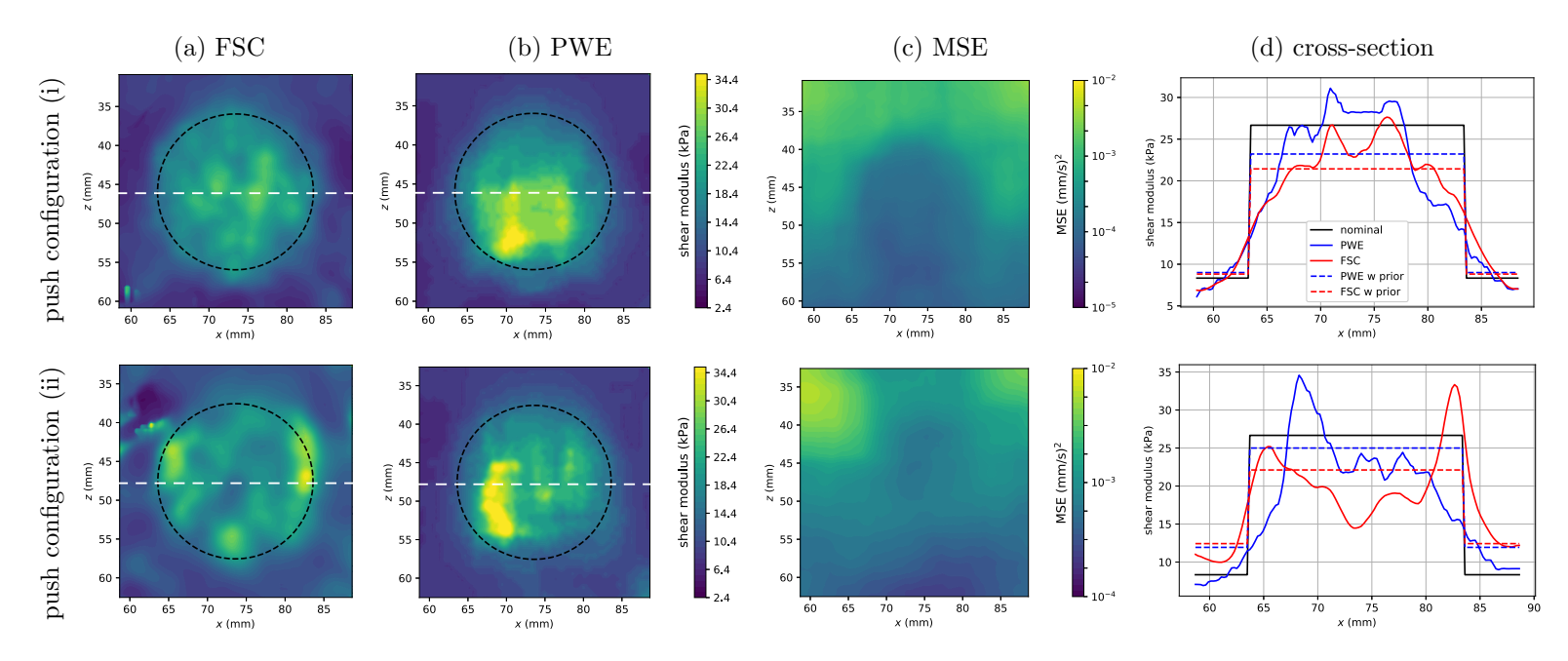


Figure 5: PWE and FSC reconstructions of the shear modulus field for the multi-push data where the results in each row correspond to one ARF configuration. Column (a) includes the FSC reconstructions whereas column (b) includes the PWE reconstructions. Column (c) plots the MSE feedback (10) corresponding to the PWE reconstructions. In column (d) we compare the estimated shear modulus fields without and with the prior knowledge of inclusion geometry, to the nominal values along the horizontal line passing through the center of the ROI, depicted by the white dashed lines in the shear modulus contour plots.

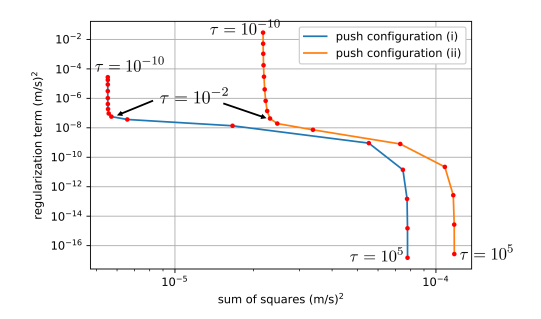


Figure 6: L-curves for the multi-push data with the two ARF configurations. The ideal value of the regularization parameter is the point of maximum inflection corresponding to  $\tau=10^{-2}$  for both cases; see Section 3.3 for more details.

Table 1: Average shear moduli  $\mu_b$  and  $\mu_i$  for the background and inclusion and the CNR (14), for the PWE and FSC methods, corresponding to the multi-push data and Fig. 5. The nominal values for the shear moduli of background and inclusion are 8.33 kPa and 26.66 kPa, respectively.

method	push configuration (i)			push configuration (ii)		
method	$\mu_b$ (kPa)	$\mu_i$ (kPa)	CNR (dB)	$\mu_b$ (kPa)	$\mu_i$ (kPa)	CNR (dB)
PWE	$9.33 \pm 2.16$	$21.69 \pm 5.79$	6.02	$9.92 \pm 1.95$	$20.59 \pm 5.43$	5.33
FSC	$10.01 \pm 2.50$	$19.70 \pm 1.89$	8.08	$12.39 \pm 3.48$	$19.93 \pm 3.62$	3.54
PWE with prior	9.00	23.22	-	11.93	25.00	-
FSC with prior	8.82	21.43	-	12.43	22.11	-

obtained from the L-curve in Fig. 6; see Section 3.3 for details. The average shear moduli are  $\mu_b = 9.33 \pm 2.16 \,\mathrm{kPa}$  and  $\mu_i = 21.69 \pm 5.79 \,\mathrm{kPa}$  and the contrast-to-noise ratio (14) is CNR = 6.02 dB; see Table 1 for a summary of the estimated shear modulus values for the reconstructions of this section. Given the prior knowledge of inclusion geometry from the B-mode image in Fig. 4, we get more accurate estimates  $\mu_b = 9.00 \,\mathrm{kPa}$  and  $\mu_i = 23.22 \,\mathrm{kPa}$ , where we use settings similar to the previous reconstruction and set  $\tau = 10^{-2}$  from the L-curve analysis; see Section 3.4 for details. Note that in this case, a scalar estimation is obtained for the background and inclusion; as a result, the standard deviation is zero and the CNR is infinite.

The contour plot in column (a) of Fig. 5 shows the corresponding FSC reconstruction for push configuration (i). To obtain the FSC estimate, using directional filters we decompose the shear wave into four directional waves traveling along angles  $-32.1^{o}$ ,  $-26.6^{o}$ ,  $206.6^{o}$ , and  $212.1^{o}$ , and rely on a radial filter to enhance the SNR. We use window and patch sizes of  $3.83 \, \mathrm{mm}$  and  $3.59 \, \mathrm{mm}$ , respectively. After constructing the shear modulus estimates for the individual waves, we combine them using compounding; see (Song et al. 2014) for details. The average shear moduli in this case are  $\mu_b = 10.01 \pm 2.50 \, \mathrm{kPa}$  and  $\mu_i = 19.70 \pm 1.89 \, \mathrm{kPa}$  and the contrast-to-noise ratio (14) is CNR =  $8.08 \, \mathrm{dB}$ . We also performed a reconstruction given the prior knowledge of the geometry, where we average the values from windows that completely fall within the background or inclusion. Using a similar window size, we get the improved estimates  $\mu_b = 8.82 \, \mathrm{kPa}$  and  $\mu_i = 21.43 \, \mathrm{kPa}$ .

The plots in the second row of Fig. 5 depict the reconstructions for push configuration (ii). This ARF configuration results in a wider frequency range at the expense of lower SNR which requires larger window sizes for acceptable

reconstructions. For PWE, we use  $f_{\rm min}=100\,{\rm Hz}$  and  $w=10.54\,{\rm mm}$  and  $\tau=10^{-2}$  from Fig. 6, resulting in  $\mu_b=9.92\pm1.95\,{\rm kPa}$  and  $\mu_i=20.59\pm5.43\,{\rm kPa}$  and CNR = 5.33 dB. Relying on the prior knowledge of inclusion geometry and with  $\tau=10^{-3}$  obtained from the L-curve analysis, we get  $\mu_b=11.93\,{\rm kPa}$  and  $\mu_i=25.00\,{\rm kPa}$ . It can be seen that using the prior knowledge improves the estimation inside the inclusion but deteriorates it for the background. This is due to the fact that parts of the background have higher noise levels and solving the SWE problem (7) only once, lumps all measurements into a single estimate. In practice it might be beneficial to decompose the background into multiple subdomains.

Plots in column (c) of Fig. 5 show the MSE (10) feedback from the PWE method for the two ARF configurations. Note the higher variations in background MSE values for both cases. Note also that the values for configuration (ii) are an order of magnitude higher indicating further inconsistency with the physics of the wave propagation. This lower SNR is also evident from Fig. 6 where the L-curve for configuration (ii) is shifted to the right (higher sum of squares).

Finally, column (a) in the second row of Fig. 5 shows the FSC reconstruction where we perform similar filtering procedures to decompose the wave and improve the SNR. With window and patch sizes of 4.31 mm and 4.07 mm, we get  $\mu_b = 12.39 \pm 3.48$  kPa and  $\mu_i = 19.93 \pm 3.62$  kPa and CNR = 3.54 dB. Relying on the prior knowledge of the geometry and with window and patch sizes of 2.87 mm and 2.64 mm, we get  $\mu_b = 12.43$  kPa and  $\mu_i = 22.11$  kPa. It seems that in these experiments, PWE reconstructions are more accurate, and the performance of the FSC method degrades more with noise than the PWE method; similar behavior was observed for other data with similar push configuration.

# 4.3. Parallel Double-push CIRS Phantoms

In this section, we consider phantoms with two parallel ARF pushes applied using a Verasonics V1 system with a L7-4 transducer (Philips Healthcare, Andover, MA) on the sides of the phantom at 30 mm focal depth. Specifically, we consider a homogeneous phantom with nominal background shear modulus of 8.33 kPa (Model 039, CIRS, Inc., Norfolk, VA), a soft Type I cylindrical inclusion with diameter 10.40 mm and nominal shear modulus of 2.66 kPa, and three stiff Type IV cylindrical inclusions with diameters 10.40 mm, 6.49 mm, and 4.05 mm and nominal shear modulus of 26.66 kPa (Model 049A, CIRS, Inc., Norfolk, VA). The push duration was 400  $\mu$ s and the push frequency was 4.09 MHz. The push beams were generated by 32 active elements located at the edges of L7-4 probe. Fig. 7 shows the B-mode image for the phantom with inclusion size of 6.49 mm along with the position of the push beams and the 16 mm×16 mm ROI. The spatial spacing of the shear wave data was 154  $\mu$ m while the temporal intervals were 240  $\mu$ s and 80  $\mu$ s for the homogeneous phantom and with inclusions, respectively. The duration of the signal was 10 ms in all cases.

Fig. 8 shows the reconstructions for both PWE and FSC methods over a  $16 \text{ mm} \times 16 \text{ mm}$  ROI without and with the prior knowledge of inclusion geometry, while Table 2 reports the corresponding average shear moduli and CNR values (14). For the PWE reconstructions, by inspecting the Fourier spectrums, for all cases except for the soft inclusion, we set the minimum frequency to  $f_{\min} = 500 \text{ Hz}$ , for the soft inclusion we set  $f_{\min} = 100 \text{ Hz}$ , and the window size to w = 3.70 mm in all cases. In each case, the regularization parameter  $\tau$  is selected according to an L-curve similar

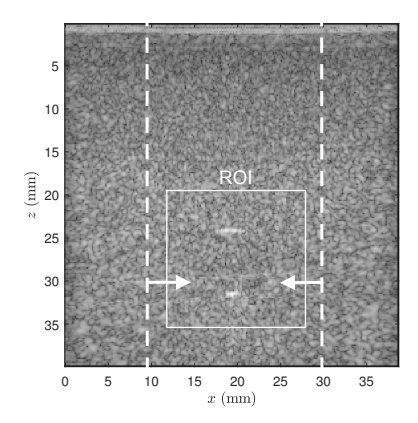


Figure 7: The geometry of the Type IV CIRS phantom and the location of the  $6.49\,\mathrm{mm}$  cylindrical inclusion for the parallel double-push case. The dashed lines delineate the approximate locations of the two push beams while the arrows show the directions of propagation and the approximate focal depths  $(30\,\mathrm{mm})$  along the push beam axes. The rectangular box depicts the  $16\,\mathrm{mm} \times 16\,\mathrm{mm}$  ROI.

Table 2: Average shear moduli  $\mu_b$  and  $\mu_i$  for the background and inclusion and the CNR (14), for the PWE and FSC methods, corresponding to the double-push data and Fig. 8. The nominal values for the shear moduli of background and soft and stiffer inclusions are 8.33 kPa, 2.66 kPa, and 26.66 kPa.

	homogeneous	soft inclusion (10.40 mm)			stiff inclusion (10.40 mm)		
method	$\mu_b$	$\mu_b$	$\mu_i$	CNR	$\mu_b$	$\mu_i$	CNR
	(kPa)	(kPa)	(kPa)	(dB)	(kPa)	(kPa)	(dB)
PWE	$5.22 \pm 0.00$	$7.17 \pm 1.94$	$3.93 \pm 1.11$	3.20	$10.69 \pm 2.88$	$25.89 \pm 4.53$	9.04
FSC	$5.32 \pm 0.20$	$7.86 \pm 2.73$	$4.11 \pm 1.29$	1.88	$11.24 \pm 3.81$	$25.62 \pm 2.97$	9.47
PWE with prior	5.17	6.03	3.31	-	10.12	28.77	-
FSC with prior	5.27	7.07	3.02	-	8.42	27.63	-
	-	stiff inclusion (6.49 mm)			stiff inclusion (4.05 mm)		
method	-	$\mu_b$	$\mu_i$	CNR	$\mu_b$	$\mu_i$	CNR
	-	(kPa)	(kPa)	(dB)	(kPa)	(kPa)	(dB)
PWE	-	$8.72 \pm 2.07$	$21.92 \pm 3.58$	10.07	$8.10 \pm 1.57$	$17.71 \pm 2.90$	9.30
FSC	-	$8.95 \pm 2.23$	$20.81 \pm 2.72$	10.56	$8.01 \pm 1.16$	$15.46 \pm 1.80$	10.84
PWE with prior	-	8.46	24.10	-	7.94	22.35	-
FSC with prior	-	7.71	22.11	-	7.76	17.39	-

Table 3: Regularization parameter  $\tau$ , selected by the L-curve analysis, for the PWE reconstructions in Fig. 8 corresponding to the double-push data.

inclusion type	without prior	with prior	
homogeneous	$10^{-3}$	$10^{-2}$	
soft inclusion (10.40 mm)	$10^{-2}$	$10^{-3}$	
stiff inclusion (10.40 mm)	$10^{-2}$	$10^{-1}$	
stiff inclusion (6.49 mm )	$10^{-3}$	$10^{-2}$	
stiff inclusion (4.05 mm)	$10^{-6}$	$10^{-6}$	

to Fig. 6; see Table 3 for numerical values. For the FSC method, we use window and patch sizes of 1.85 mm and 1.69 mm, respectively. Note that as in the previous

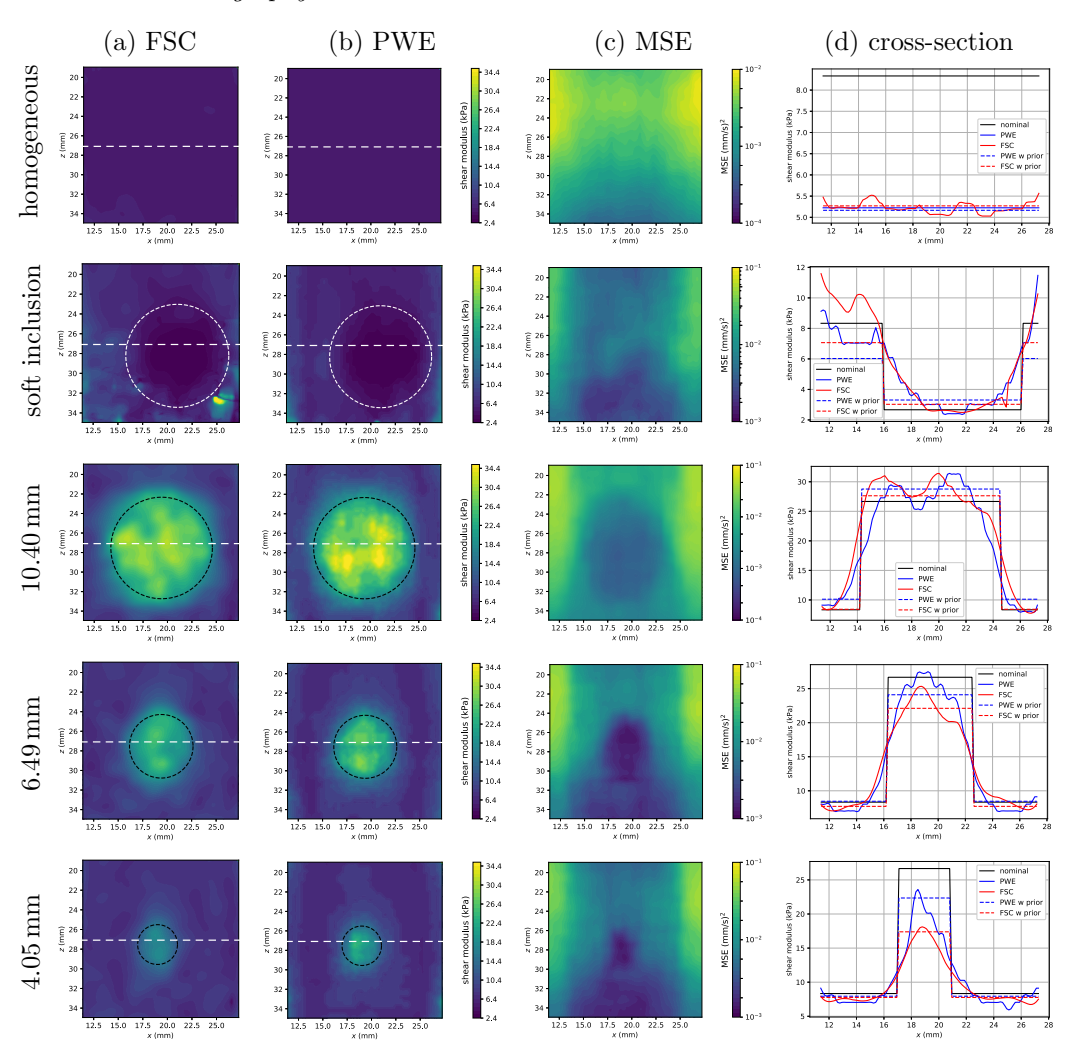
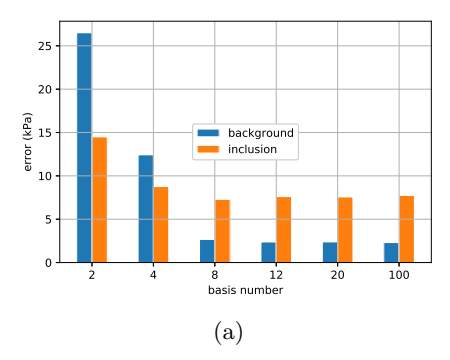


Figure 8: PWE and FSC reconstructions for the double-push phantom data with a soft Type I inclusion and three stiff Type IV inclusions. Each row includes the reconstructions for one inclusion. Columns (a) and (b) include the FSC and PWE reconstructions, respectively. Column (c) plots the MSE feedback (10) corresponding to the PWE reconstructions. In column (d) we compare the estimated shear modulus fields without and with the prior knowledge of inclusion geometry, to the nominal values along the horizontal line passing through the center of the ROI, depicted by the white dashed lines in the shear modulus contour plots.

cases, the PWE method is unaware of the directions of propagation. Nevertheless, the PWE reconstructions without prior directional filtering are competitive with the FSC method and often more accurate, when compared to the nominal values reported by the manufacturer. For the homogeneous case in the first row of Fig. 8, the estimates are not in agreement with the nominal values due possibly to the change in mechanical properties of the phantom over time<sup>5</sup> (Baghani et al. 2011) but the PWE and FSC estimates are in agreement with each other. From Table 2, observe that

<sup>5</sup> The homogeneous phantom was manufactured before April 12, 2014 and is over six years old.



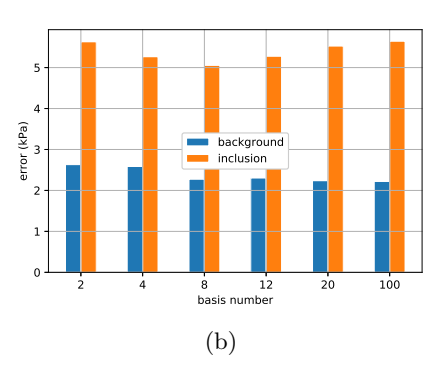


Figure 9: Absolute errors of the average background and inclusion shear moduli as a function of the basis number  $n_b$ . (a) Fig. 9a corresponds to the multi-push data of Section 4.2 with push configuration (i). (b) Fig. 9b corresponds to the double-push data of Section 4.3 for inclusion diameter of 6.49 mm.

the FSC reconstructions have slightly better CNR values due to compounding, which naturally increases the CNR because of averaging and reduced variance. Also, the reconstructions with prior knowledge of the geometry often lead to a better contrast between the background and inclusion.

## 4.4. Parameter Study

In this section, we study the effect of important parameters, discussed in Section 3.3, on PWE reconstructions. In each case, we optimally select all other parameters including the regularization parameter. First, we consider the effect of basis number  $n_b$  on PWE reconstructions. In Fig. 9, we plot the absolute errors of  $\mu_b$  and  $\mu_i$ compared to the nominal values for the multi-push data with push configuration (i), and the double-push data with 6.49 mm inclusion size, discussed in Sections 4.2 and 4.3, respectively. From Fig. 9a corresponding to the multi-push data, it can be seen that  $n_b = 2, 4$  are insufficient to resolve the shear wave particularly in the background. but the reconstructions seem to plateau beyond  $n_b = 8$ . Unlike the multi-push data, it can be seen from Fig. 9b that for the double-push data, only two basis functions are adequate since these two bases happen to align with the directions of propagation. In both cases, because of appropriate regularization, the solutions stay stable as we keep increasing the number of basis functions. Note that throughout the results, we used  $n_b = 12$  bases to reconstruct the shear modulus fields although the true propagation directions might not align with such a sparse discretization. This indicates that PWE can reconstruct the shear modulus field even if the dominant propagation directions are not fully recovered. In Appendix B, we further elaborate on this point.

To study the rest of the important parameters for PWE, we consider the doublepush data with 6.49 mm inclusion as a representative example. First, we investigate the effect of the number of frequency  $n_{\omega}$  and minimum frequency  $f_{\min}$  on CNR (14) and normalized error, defined as  $\text{err} = \|\mu - \mu^{\text{nom}}\|/\|\mu^{\text{nom}}\|$ , where  $\mu$  is the output of PWE Algorithm 1 and  $\mu^{\text{nom}}$  is the corresponding nominal vector of values. Fig. 10 shows the results for three different frequency numbers  $n_{\omega}$  and a range of minimum frequency  $f_{\min}$  values. As discussed in Section 3.3, increasing  $n_{\omega}$  and  $f_{\min}$  generally leads to better reconstructions. However, there is a value of  $f_{\min}$  above which the selected frequencies mostly contain noise and are not as informative; this is the reason for upward trend in Fig. 10a for large values of  $f_{\min}$ . This upward trend starts earlier

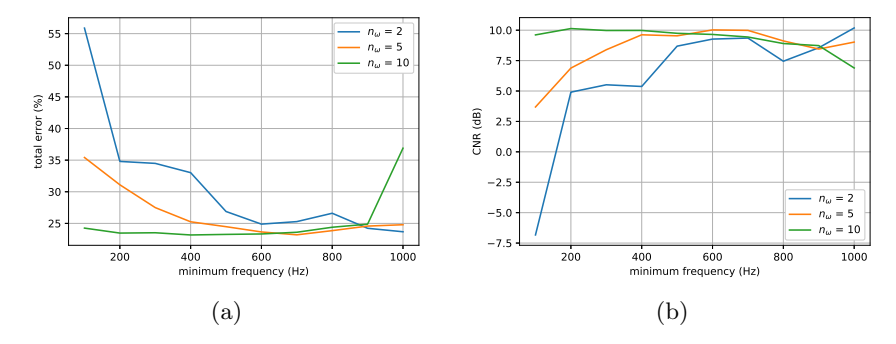


Figure 10: (a) Fig. 10a plots the normalized  $\ell_2$ -error over the ROI as a function of the frequency lower-bound  $f_{\min}$  for three different number of dominant frequencies  $n_{\omega}$ . (b) Fig. 10b shows the similar plot for the CNR (14). Generally using larger  $n_{\omega}$  and  $f_{\min}$  improves both the error and CNR.

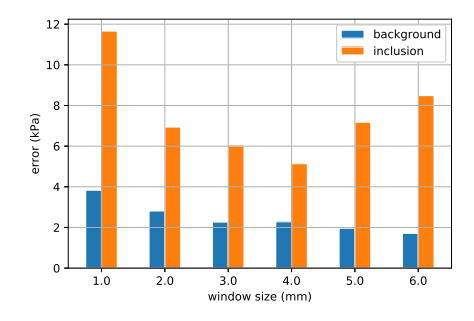


Figure 11: Absolute errors of the average background and inclusion shear moduli as a function of the window size w for the double-push data of Section 4.3 with inclusion diameter of 6.49 mm.

for larger  $n_{\omega}$  since given a large value of  $f_{\min}$ , using more frequencies, leads to earlier inclusion of higher frequency noisy data.

Finally, we study the effect of window size w. Fig. 11 shows a bar plot similar to Fig. 9, where we compare the average estimates in the background and inclusion to the nominal values. As discussed in Section 3.3, overly small values of w, compared to the wavelength corresponding to  $f_{\min}$ , cannot resolve the waves and result in poor reconstructions. On the other hand, large values of w result in over-smoothed, poor reconstructions. This can be seen here for the estimation of the inclusion shear modulus. Note that among the parameters studied in this section, the error values are more sensitive to window size w and minimum frequency  $f_{\min}$ . Since for a given dataset, the range of dominant frequencies  $[f_{\min}, f_{\max}]$  is determined, to obtain reasonable reconstructions, we need to adjust w; the lower  $f_{\min}$ , the larger w needs to be for accurate reconstruction; see Section 3.3.

# 5. Discussion

The PWE Algorithm 1 depends on a number of parameters. Among those, the number of dominant frequencies and plane wave basis functions can generally be fixed, as in Section 4. The frequency range  $[f_{\min}, f_{\max}]$  is dictated by the shear wave data and should be selected by inspecting the Fourier spectrum and the knowledge of  $f_{\min}$  enables the selection of window size w, as discussed in Section

3.3. Ultimately, the only parameter that needs to be tuned in practice is the regularization parameter  $\tau$  for which we outlined the L-curve approach in Section 3.3. Moreover, unlike the reconstructions in Section 4 which are based on data obtained from acquisitions with different settings, in practice the PWE algorithm will be used on an ultrasound system with consistent acquisition settings and noise characteristics. Under these circumstances, all of the parameters including  $\tau$  can often be pre-selected. For instance, observe the consistency among parameters used for double-push reconstructions of Section 4.3. Finally, the FSC method (Song et al. 2014) used for validation in Section 4, requires selecting at least as many parameters. These include the propagation directions, window and patch sizes, and parameters of the directional and radial filters including temporal and spatial frequency ranges, and power and order; see Appendix A.

As we discussed in Section 4.4, when the plane wave directions in (4) happen to align with the propagation direction, PWE can reconstruct the shear modulus field with a few basis functions; see Fig. 9b. This means that we can exploit the prior knowledge of propagation directions if available, by using a non-uniform distribution on the directions instead of the uniform distribution in (12). PWE can also be utilized with prior filtering and compounding, similar to the FSC method. When multiple sets of data from independent experiments are available, instead of compounding, we can also (i) extend the optimization objective in (7) to include another summation over these sets of data, or (ii) superpose the data and process them at once as a single multi-push data.

As discussed in Section 3.1, the MSE is only reliable if precautions are taken to prevent overfitting by appropriately selecting the regularization parameter. Throughout the paper, we used a constant regularization parameter for each reconstruction, selected using the L-curve approach, that on average best balances the least-squares and regularization terms over the ROI; see Section 3.3 for details. This value of regularization parameter might not prevent overfitting in local regions that are considerably noisier than the rest of the ROI. An example of this can be found in the reconstructions of Figure 5 where overestimation of the shear modulus inside inclusions is not reflected in the corresponding MSE plots. It is possible but computationally expensive and often unnecessary, to tune the regularization parameter for individual windows.

The computational cost of the PWE Algorithm 1 depends on the basis number  $n_b$ , the measurement number m, the number of frequencies  $n_\omega$ , method used to solve (9), and the number of subdomains  $n_s$ . From (8), it can be seen that the dependence on the number of bases and measurements is  $O(m n_b^2 + n_b^3)$  in the worst case while from (9), dependence on  $n_{\omega}$  is linear. Assuming we use a simple discretization of the feasible wave-speed range  $[c_{\min}, c_{\max}]$  with  $n_c$  points to approximately solve (9), dependence on  $n_c$  is also linear. Thus, the worst case computational cost of solving (7) for a homogeneous subdomain is bounded by  $O(n_b^2(m+n_b)n_\omega n_c)$ . From Algorithm 1, observe that there is an explicit loop over the  $n_s$  subdomains. Thus, the worst case computational cost of the PWE algorithm is bounded by  $O(n_b^2(m+n_b)n_\omega n_c n_s)$ . Nevertheless, the optimal coefficients for different frequencies can be calculated independently and in parallel using (8). Moreover, the solution for each subdomain is independent and can be parallelized. Thus, the effective cost is only bounded by  $O(n_b^2(m+n_b)n_c)$ . Note that the window size w affects the computational cost through the number of measurements m and dependence on the regularization parameter  $\tau$ is negligible. The reconstructions reported in this paper typically require less than a minute on a desktop computer with an INTEL Core i9-3.10 GHz processor and 128 GB of memory, using our initial implementation of PWE. This computation time could however be considerably improved due the highly parallelizable nature of PWE and particularly, by utilizing GPUs to solve the linear system in (8).

The proposed PWE method has potential in other elastography approaches particularly in those that use vibration for excitation resulting in complicated motion fields that cannot easily be directionally decoupled. This includes magnetic resonance elastography (Muthupillai et al. 1995), vibration-based ultrasound elastography (Zhao et al. 2014), passive ultrasound elastography (Catheline et al. 2008, Brum et al. 2015), and optical coherence elastography (Liu et al. 2020b, Liu et al. 2020a).

Finally, processing in vivo patient data poses new challenges that we plan to investigate. This includes the viscoelastic nature of the soft tissue, as opposed to the elastic assumption made in this paper, and significantly higher noise levels due to physiological movement, severe inhomogeneity of the soft tissue, and dissipation caused by viscosity. As we demonstrated in Section 4.2, PWE seems to be more robust to noise than FSC and has potential for even more improvement when applied to in vivo data with low SNR. It is known that in addition to the shear modulus, the shear viscosity of soft tissue also has diagnostic value (Kumar et al. 2018). PWE can be extended to estimate the shear viscosity by considering a complex modulus in wave equation (2) and conducting a 2D search instead of the line search in (9).

#### 6. Conclusion

We proposed PWE, a novel ultrasound SWE approach that unlike commonly used techniques, can handle multiple waves with arbitrary incident angles at once and does not rely on directionality of the propagation or the prior knowledge of the propagation direction. We demonstrated through various phantom studies that PWE can reconstruct the shear modulus field with an accuracy comparable to state-of-the-art and provide feedback on the reconstruction. When the prior knowledge of the inclusion geometry was available, we obtained more efficient and accurate reconstructions.

## Acknowledgments

This work is supported in part by the National Science Foundation under grant CNS #1837499.

# References

- Alnaes, M., Blechta, J., Hake, J., Johansson, A., Kehlet, B., Logg, A., Richardson, C., Ring, J., Rognes, M. E. & Wells, G. N. (2015). The fenics project version 1.5, Archive of Numerical Software 3(100).
- Aquino, W. & Bonnet, M. (2019). Analysis of the error in constitutive equation approach for timeharmonic elasticity imaging, SIAM Journal on Applied Mathematics 79(3): 822–849.
- Athanasiou, A., Tardivon, A., Tanter, M., Sigal-Zafrani, B., Bercoff, J., Deffieux, T., Gennisson, J.-L., Fink, M. & Neuenschwander, S. (2010). Breast lesions: quantitative elastography with supersonic shear imaging—preliminary results, *Radiology* **256**(1): 297–303.
- Baghani, A., Salcudean, S., Honarvar, M., Sahebjavaher, R. S., Rohling, R. & Sinkus, R. (2011). Travelling wave expansion: a model fitting approach to the inverse problem of elasticity reconstruction, *IEEE Transactions on Medical Imaging* 30(8): 1555–1565.

- Barr, R. G. & Zhang, Z. (2015). Shear-wave elastography of the breast: value of a quality measure and comparison with strain elastography, Radiology 275(1): 45–53.
- Bercoff, J., Tanter, M. & Fink, M. (2004). Supersonic shear imaging: a new technique for soft tissue elasticity mapping, *IEEE transactions on ultrasonics, ferroelectrics, and frequency control* **51**(4): 396–409.
- Brum, J., Catheline, S., Benech, N. & Negreira, C. (2015). Quantitative shear elasticity imaging from a complex elastic wavefield in soft solids with application to passive elastography, *IEEE Transactions on Ultrasonics, Ferroelectrics, and Frequency Control* **62**(4): 673–685.
- Budelli, E., Brum, J., Bernal, M., Deffieux, T., Tanter, M., Lema, P., Negreira, C. & Gennisson, J.-L. (2016). A diffraction correction for storage and loss moduli imaging using radiation force based elastography, *Physics in Medicine & Biology* 62(1): 91.
- Carrascal, C. A., Chen, S., Manduca, A., Greenleaf, J. F. & Urban, M. W. (2017). Improved shear wave group velocity estimation method based on spatiotemporal peak and thresholding motion search, *IEEE transactions on ultrasonics, ferroelectrics, and frequency control* 64(4): 660–668.
- Catheline, S., Benech, N., Brum, J. & Negreira, C. (2008). Time reversal of elastic waves in soft solids, *Physical review letters* 100(6): 064301.
- Chen, S., Fatemi, M. & Greenleaf, J. F. (2004). Quantifying elasticity and viscosity from measurement of shear wave speed dispersion, The Journal of the Acoustical Society of America 115(6): 2781–2785.
- Chen, S., Urban, M. W., Pislaru, C., Kinnick, R., Zheng, Y., Yao, A. & Greenleaf, J. F. (2009). Shearwave dispersion ultrasound vibrometry (SDUV) for measuring tissue elasticity and viscosity, IEEE transactions on ultrasonics, ferroelectrics, and frequency control 56(1): 55–62.
- Colton, D. & Kress, R. (2001). On the denseness of Herglotz wave functions and electromagnetic Herglotz pairs in sobolev spaces, Mathematical methods in the applied sciences 24(16): 1289– 1303.
- Deffieux, T., Gennisson, J.-L., Bercoff, J. & Tanter, M. (2011). On the effects of reflected waves in transient shear wave elastography, *IEEE transactions on ultrasonics*, ferroelectrics, and frequency control **58**(10): 2032–2035.
- Deng, Y., Rouze, N. C., Palmeri, M. L. & Nightingale, K. R. (2016). Ultrasonic shear wave elasticity imaging sequencing and data processing using a Verasonics research scanner, *IEEE transactions on ultrasonics, ferroelectrics, and frequency control* **64**(1): 164–176.
- Denis, M., Mehrmohammadi, M., Song, P., Meixner, D. D., Fazzio, R. T., Pruthi, S., Whaley, D. H., Chen, S., Fatemi, M. & Alizad, A. (2015). Comb-push ultrasound shear elastography of breast masses: Initial results show promise, *PloS one* 10(3): e0119398.
- Eskandari, H., Salcudean, S. E., Rohling, R. & Ohayon, J. (2008). Viscoelastic characterization of soft tissue from dynamic finite element models, *Physics in Medicine & Biology* **53**(22): 6569.
- Gerber, L., Fitting, D., Srikantharajah, K., Weiler, N., Kyriakidou, G., Bojunga, J., Schulze, F., Bon, D., Zeuzem, S. & Friedrich-Rust, M. (2017). Evaluation of 2D-shear wave elastography for characterisation of focal liver lesions., *Journal of Gastrointestinal & Liver Diseases* 26(3).
- Ghosh, S., Zou, Z., Babaniyi, O., Aquino, W., Diaz, M. I., Bayat, M. & Fatemi, M. (2017). Modified error in constitutive equations (MECE) approach for ultrasound elastography, *The Journal* of the Acoustical Society of America 142(4): 2084–2093.
- Hansen, P. C. (2010). Discrete Inverse Problems, SIAM.
- Honarvar, M., Sahebjavaher, R. S., Rohling, R. & Salcudean, S. E. (2017). A comparison of finite element-based inversion algorithms, local frequency estimation, and direct inversion approach used in mre, *IEEE transactions on medical imaging* **36**(8): 1686–1698.
- Itoh, A., Ueno, E., Tohno, E., Kamma, H., Takahashi, H., Shiina, T., Yamakawa, M. & Matsumura, T. (2006). Breast disease: clinical application of US elastography for diagnosis, *Radiology* **239**(2): 341–350.
- Kasai, C., Namekawa, K., Koyano, A. & Omoto, R. (1985). Real-time two-dimensional blood flow imaging using an autocorrelation technique, *IEEE Transactions on sonics and ultrasonics* 32(3): 458–464.
- Khodayi-mehr, R., Urban, M. W., Zavlanos, M. M. & Aquino, W. (2020). Movie of vertical shear wave velocity for multi-push data. <a href="https://vimeo.com/442567542">https://vimeo.com/442567542</a>.
- Kijanka, P., Qiang, B., Song, P., Carrascal, C. A., Chen, S. & Urban, M. W. (2018). Robust phase velocity dispersion estimation of viscoelastic materials used for medical applications based on the multiple signal classification method, *IEEE transactions on ultrasonics*, ferroelectrics, and frequency control 65(3): 423–439.
- Kijanka, P. & Urban, M. W. (2018). Local phase velocity based imaging: A new technique used for

- ultrasound shear wave elastography, IEEE transactions on medical imaging 38(4): 894–908.
- Kumar, V., Denis, M., Gregory, A., Bayat, M., Mehrmohammadi, M., Fazzio, R., Fatemi, M. & Alizad, A. (2018). Viscoelastic parameters as discriminators of breast masses: Initial human study results, PloS one 13(10): e0205717.
- Lipman, S. L., Rouze, N. C., Palmeri, M. L. & Nightingale, K. R. (2016). Evaluating the improvement in shear wave speed image quality using multidimensional directional filters in the presence of reflection artifacts, *IEEE transactions on ultrasonics, ferroelectrics, and frequency control* 63(8): 1049–1063.
- Liu, H.-C., Kijanka, P. & Urban, M. W. (2020a). Four-dimensional (4D) phase velocity optical coherence elastography in heterogeneous materials and biological tissue, *Biomedical Optics Express* 11(7): 3795–3817.
- Liu, H.-C., Kijanka, P. & Urban, M. W. (2020b). Optical coherence tomography for evaluating capillary waves in blood and plasma, *Biomedical Optics Express* 11(2): 1092–1106.
- Liu, S., Wu, X.-D., Xu, W.-J., Lin, Q., Liu, X.-J. & Li, Y. (2016). Is there a correlation between the presence of a spiculated mass on mammogram and luminal a subtype breast cancer?, Korean journal of radiology 17(6): 846–852.
- Manduca, A., Lake, D. S., Kruse, S. A. & Ehman, R. L. (2003). Spatio-temporal directional filtering for improved inversion of MR elastography images, *Medical image analysis* 7(4): 465–473.
- McLaughlin, J. & Renzi, D. (2006). Using level set based inversion of arrival times to recover shear wave speed in transient elastography and supersonic imaging, *Inverse Problems* **22**(2): 707.
- Mehrmohammadi, M., Song, P., Meixner, D. D., Fazzio, R. T., Chen, S., Greenleaf, J. F., Fatemi, M. & Alizad, A. (2014). Comb-push ultrasound shear elastography (CUSE) for evaluation of thyroid nodules: preliminary in vivo results, *IEEE transactions on medical imaging* 34(1): 97–106.
- Muthupillai, R., Lomas, D., Rossman, P., Greenleaf, J. F., Manduca, A. & Ehman, R. L. (1995).
  Magnetic resonance elastography by direct visualization of propagating acoustic strain waves, science 269(5232): 1854–1857.
- Palmeri, M. L., Qiang, B., Chen, S. & Urban, M. W. (2016). Guidelines for finite-element modeling of acoustic radiation force-induced shear wave propagation in tissue-mimicking media, *IEEE transactions on ultrasonics*, ferroelectrics, and frequency control 64(1): 78–92.
- Palmeri, M. L., Wang, M. H., Dahl, J. J., Frinkley, K. D. & Nightingale, K. R. (2008). Quantifying hepatic shear modulus in vivo using acoustic radiation force, *Ultrasound in medicine & biology* **34**(4): 546–558.
- Park, E. & Maniatty, A. M. (2006). Shear modulus reconstruction in dynamic elastography: time harmonic case, *Physics in Medicine & Biology* **51**(15): 3697.
- Parker, K. J., Ormachea, J., Zvietcovich, F. & Castaneda, B. (2017). Reverberant shear wave fields and estimation of tissue properties, *Physics in Medicine & Biology* **62**(3): 1046.
- Rouze, N. C., Wang, M. H., Palmeri, M. L. & Nightingale, K. R. (2012). Parameters affecting the resolution and accuracy of 2-D quantitative shear wave images, *IEEE transactions on ultrasonics*, ferroelectrics, and frequency control 59(8): 1729–1740.
- Sarvazyan, A. P., Urban, M. W. & Greenleaf, J. F. (2013). Acoustic waves in medical imaging and diagnostics. *Ultrasound in medicine & biology* **39**(7): 1133–1146.
- Shiina, T., Nightingale, K. R., Palmeri, M. L., Hall, T. J., Bamber, J. C., Barr, R. G., Castera, L., Choi, B. I., Chou, Y.-H., Cosgrove, D. et al. (2015). WFUMB guidelines and recommendations for clinical use of ultrasound elastography: Part 1: basic principles and terminology, Ultrasound in medicine & biology 41(5): 1126–1147.
- Sigrist, R. M., Liau, J., El Kaffas, A., Chammas, M. C. & Willmann, J. K. (2017). Ultrasound elastography: review of techniques and clinical applications, Theranostics 7(5): 1303.
- Song, P., Macdonald, M. C., Behler, R. H., Lanning, J. D., Wang, M. H., Urban, M. W., Manduca, A., Zhao, H., Callstrom, M. R., Alizad, A. et al. (2015). Two-dimensional shear-wave elastography on conventional ultrasound scanners with time-aligned sequential tracking (tast) and comb-push ultrasound shear elastography (cuse), IEEE transactions on ultrasonics, ferroelectrics, and frequency control 62(2): 290–302.
- Song, P., Manduca, A., Zhao, H., Urban, M. W., Greenleaf, J. F. & Chen, S. (2014). Fast shear compounding using robust 2-D shear wave speed calculation and multi-directional filtering, Ultrasound in medicine & biology 40(6): 1343–1355.
- Song, P., Zhao, H., Manduca, A., Urban, M. W., Greenleaf, J. F. & Chen, S. (2012). Comb-push ultrasound shear elastography (CUSE): a novel method for two-dimensional shear elasticity imaging of soft tissues, *IEEE transactions on medical imaging* **31**(9): 1821–1832.
- Tanter, M., Bercoff, J., Athanasiou, A., Deffieux, T., Gennisson, J.-L., Montaldo, G., Muller, M., Tardivon, A. & Fink, M. (2008). Quantitative assessment of breast lesion viscoelasticity:

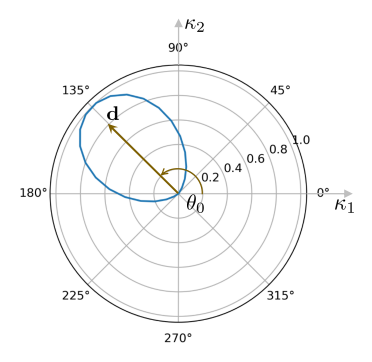


Figure A1: Polar plot of the directional filter  $\max[0,\cos(\theta-\theta_0)]^2$  in the  $\kappa_1 - \kappa_2$  plane for  $\theta_0 = 135^o$ , where  $\mathbf{d} \in \mathbb{R}^2$  denotes the unit direction vector corresponding to the propagation direction  $\theta_0$ . The filter peaks at  $\theta_0$  and quickly decays for directions far from  $\theta_0$ . Particularly, it equals zero for any direction with  $|\theta - \theta_0| > 90^o$ , meaning that reflections are mostly filtered.

initial clinical results using supersonic shear imaging, Ultrasound in medicine & biology 34(9): 1373–1386.

Urban, M. W. & Greenleaf, J. F. (2008). Harmonic pulsed excitation and motion detection of a vibrating reflective target, The Journal of the Acoustical Society of America 123(1): 519– 533.

van Sloun, R. J., Wildeboer, R. R., Wijkstra, H. & Mischi, M. (2017). Viscoelasticity mapping by identification of local shear wave dynamics, *IEEE transactions on ultrasonics, ferroelectrics, and frequency control* **64**(11): 1666–1673.

Zhao, H., Song, P., Meixner, D. D., Kinnick, R. R., Callstrom, M. R., Sanchez, W., Urban, M. W., Manduca, A., Greenleaf, J. F. & Chen, S. (2014). External vibration multi-directional ultrasound shearwave elastography (EVMUSE): Application in liver fibrosis staging, *IEEE transactions on medical imaging* 33(11): 2140–2148.

#### Appendix A. Connection to Directional Filter

In Section 1, we discussed the importance of directional filtering to time-of-flight (ToF) methods. Here we discuss the connection between directional filtering and the PWE method. The directional filter operates on the 3D Fourier transformed signal in the spatial frequency domain. Let  $\kappa_1$  and  $\kappa_2$  denote the components of spatial frequency (wavenumber). Given a propagation direction  $\theta_0$ , the directional filter is defined in the  $\kappa_1 - \kappa_2$  plane as  $\max[0, \cos(\theta - \theta_0)]^p$ , where  $\theta$  denotes the angle in polar coordinates and the power p is a parameter to be chosen; in (Manduca et al. 2003),  $2 \le p \le 3$ . Fig. A1 depicts the directional filter for  $\theta_0 = 135^o$ . This filter is applied across all positive temporal frequencies  $\omega > 0$ . For negative frequencies, the direction needs to be reversed since those waves travel backward in time. Often, a radial component is also added to improve the SNR by eliminating oscillations with unrealistically high wavenumbers. In (Manduca et al. 2003), this radial component is a bandpass Butterworth filter. As we discussed in Section 4, both the directional and radial components are essential for ToF methods.

To see the connection between the PWE method and the directional filter, observe that given a frequency  $\omega$  and for each angle  $\theta_0$ , there exists a plane wave that travels in the direction  $\mathbf{d} = [\cos \theta_0, \sin \theta_0]$ . Because ToF technique relies on directional propagation, we need to manually decompose the shear wave into its directional components specified by angles  $\theta_0$ , process each component separately, and then combine them through compounding. The PWE method on the other hand,

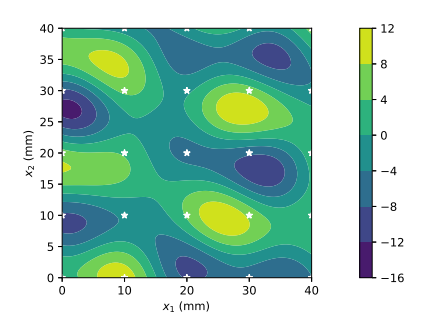


Figure B1: The real component of the fabricated data (units are arbitrary) within a homogeneous subdomain  $\Omega = [0,40] \times [0,40] \,\mathrm{mm^2}$  with wave-speed of  $c=5\,\mathrm{m/s}$  at frequency  $\omega=600\pi\,\mathrm{rad/s}$ , composed of 5 plane waves propagating at uniformly spaced angles; the wave traveling at angle  $72^o$  is dominant. The white stars indicate the grid of  $5\times5$  measurements used for elastography.

searches for dominant directions to capture the shear wave in its entirety (including the reflections and refractions) and to simultaneously compute the wave-speed that best describes the observed data at once. This removes the need for the arbitrary compounding (averaging) step<sup>6</sup> and instead selects the shear modulus value considering all data together. To improve the nonlinearity of the PWE optimization problem and at the expense of increasing the dimension of the problem being solved, we explicitly discretized the plane wave directions  $\theta_0$  in (12) to obtain a finite set of  $n_b$  plane wave basis functions given by (4). The dominance of each direction  $\mathbf{d}_j$  in capturing the shear wave is then determined by the magnitude of the corresponding basis coefficient  $a_j$ . Note that the plane waves in expansion (3) are fundamental solutions of the scalar wave equation (2) and form a complete set of basis functions meaning that by increasing  $n_b$ , we can approximate the solution to the wave equation as closely as we desire (Colton & Kress 2001).

## Appendix B. Nonlinearity of Objective Function

In this appendix, we consider more closely the ability of the PWE method to recover dominant propagation directions and the importance of this ability for reconstructing the desired shear modulus field. We also take a closer look at the shape (nonlinearity) of the objective function in (9) and how the presence of noise and absence of true propagation directions affect it. For simplicity, we use simulated data in a homogeneous medium with shear modulus of  $\mu = 25\,\mathrm{kPa}$ , amounting to a wavespeed of  $c = 5\,\mathrm{m/s}$ . We directly fabricate a frequency-domain displacement field using (3) composed of 5 plane waves propagating with uniform angular spacing of  $72^o$  at frequency  $\omega = 600\pi\,\mathrm{rad/s}$ . Fig. B1 shows the real component of the field along with a grid of  $m = 5 \times 5$  measurements used for elastography. We choose the coefficients in (3) such that the dominant propagation directions are ordered as  $[72^o, -72^o, 0^o, -144^o, 144^o]$ .

In Table B1 we study the effect of including the true propagation directions and noise on recovering the dominant propagation directions. To include the true directions, we use  $n_b = 20$  whereas to exclude them, we set  $n_b = 21$ . Furthermore, we

6 One could for instance argue for selecting the point-wise maximum of the shear modulus fields instead of averaging. There is no particular advantage to compounding via averaging.

Table B1: Effect of excluding true propagation directions and noise on recovering the dominant propagation directions using PWE for the fabricated frequency-domain displacement data.

true directions	noiseless measurements	noisy measurements		
included	$[72^o, -72^o, 0^o, -144^o, 144^o]$	$[72^o, -72^o, 0^o, 144^o, -126^o]$		
excluded	$[69^o, -34^o, 34^o, -69^o, 0^o]$	$[69^o, -34^o, 120^o, -69^o, 34^o]$		

Table B2: The estimated shear modulus value (kPa) using the PWE method for the homogeneous medium with the ground-truth value of 25 kPa.

true directions	noiseless measurements	noisy measurements
included	25.00	24.90
excluded	25.50	25.10

use additive Gaussian noise resulting in SNR = 19.92 dB. In the noiseless case, we set the regularization parameter to  $\tau=10^{-10}$  whereas in the noisy cases, we use  $\tau=10^{-2}$ . Observe that when true directions are included, in the absence of noise the true directions are exactly recovered up to their dominancy order. On the other hand, in the presence of noise the last dominant direction is not in the top five selected directions. When the true directions are excluded, the less dominant directions  $-144^o$  and  $144^o$  are not closely approximated in the top five propagation directions although plane waves close to these directions might still have high coefficients. The reason for this behavior is that  $\ell_2$ -regularization is known to result in many small coefficients. Using a regularization term in (7) that enhances sparsity helps with better recovering the dominant directions at the expense of higher computational cost but as we show next, exactly recovering these dominant directions is not necessary for accurate shear modulus estimation.

To further elaborate on the last comment, we study the performance of PWE using displacement data corresponding to two frequencies  $\omega = 600\pi \,\mathrm{rad/s}$  and  $1200\pi \,\mathrm{rad/s}$ with  $SNR = 19.92 \, dB$  and  $SNR = 21.84 \, dB$  for noisy measurements. Fig. B2 depicts the objective function in (9) for the four different cases of including or excluding true directions and noiseless or noisy data. Observe that the objective in all cases is extremely non-smooth. Also notice that the individual frequencies can have multiple local minima, some of which might have a smaller objective value than the true wavespeed. Nevertheless, the total objective function summed over the two frequencies often has its global minimum close to the true wave-speed. This shows the importance of using large number of frequencies  $n_{\omega}$  to ensure that enough information is available for reconstruction. Finally, notice that when the true directions are excluded from reconstruction or data are noisy, the global minimum becomes less prominent. Table B2 reports the estimated constant shear modulus value at each case. Note that although when the true directions are excluded, the dominant directions might not be properly identified as we observed in Table B1, the PWE method still succeeds in approximating the true shear modulus values.

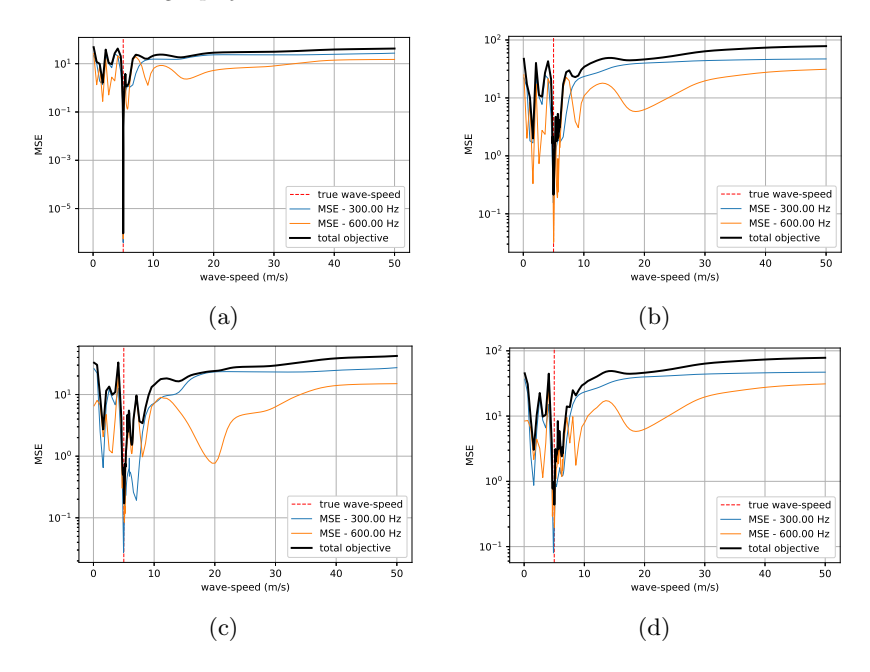


Figure B2: Objective function in (9) as a function of the constant wave-speed c (homogeneous medium) for the fabricated data with 5 plane waves at two frequencies  $\omega=600\pi\,\mathrm{rad/s}$  and  $1200\pi\,\mathrm{rad/s}$ . (a) Fig. B2a shows the objective function for the case of noiseless data when the true propagation directions are included in the bases (3). (b) Fig. B2b shows the similar plot for noisy data. Plots in the second row exclude the true propagation directions. (c,d) Fig. B2c corresponds to noiseless data whereas Fig. B2d depicts the objective for noisy data.